Inorg. Chem. **2009**, *48*, 4478−4490

Synthesis and X-ray Crystal Structure of $(OsO_3F_2)_2 \cdot 2XeOF_4$ and the Raman Spectra of $(OsO_3F_2)_\infty$, $(OsO_3F_2)_2$, and $(OsO_3F_2)_2 \cdot 2XeOF_4$

Michael J. Hughes, Hélène P. A. Mercier, and Gary J. Schrobilgen*

Department of Chemistry, McMaster University, Hamilton, Ontario, L8S 4M1, Canada

Received February 5, 2009

The adduct, $(OsO_3F_2)_2 \cdot 2XeOF_4$, was synthesized by dissolution of the infinite chain polymer, $(OsO_3F_2)_\infty$, in $XeOF_4$ solvent at room temperature followed by removal of excess $XeOF_4$ under dynamic vacuum at 0 °C. Continued pumping at 0 °C resulted in removal of associated $XeOF_4$, yielding $(OsO_3F_2)_2$, a new low-temperature phase of OsO_3F_2. Upon standing at 25 °C for $1^1/_2$ h, $(OsO_3F_2)_2$ underwent a phase transition to the known monoclinic phase, $(OsO_3F_2)_\infty$. The title compounds, $(OsO_3F_2)_\infty$, $(OsO_3F_2)_2$, and $(OsO_3F_2)_2 \cdot 2XeOF_4$ have been characterized by low-temperature (−150 °C) Raman spectroscopy. Crystallization of $(OsO_3F_2)_2 \cdot 2XeOF_4$ from $XeOF_4$ solution at 0 °C yielded crystals suitable for X-ray structure determination. The structural unit contains the $(OsO_3F_2)_2$ dimer in which the OsO_3F_3 units are joined by two Os---F---Os bridges having fluorine bridge atoms that are equidistant from the osmium centers (2.117(5) and 2.107(4) Å). The dimer coordinates to two $XeOF_4$ molecules through Os−F···Xe bridges in which the Xe···F distances (2.757(5) Å) are significantly less than the sum of the Xe and F van der Waals radii (3.63 Å). The $(OsO_3F_2)_2$ dimer has C_i symmetry in which each pseudo-octahedral OsO_3F_3 unit has a facial arrangement of oxygen ligands with $XeOF_4$ molecules that are only slightly distorted from their gas-phase C_{4v} symmetry. Quantum-chemical calculations using SVWN and B3LYP methods were employed to calculate the gas-phase geometries, natural bond orbital analyses, and vibrational frequencies of $(OsO_3F_2)_2$, $(OsO_3F_2)_2 \cdot 2XeOF_4$, $XeOF_4$, OsO_2F_4, and $(\mu\text{-}FOsO_3F_2)_2OsO_3F^-$ to aid in the assignment of the experimental vibrational frequencies of $(OsO_3F_2)_2$, $(OsO_3F_2)_2 \cdot 2XeOF_4$, and $(OsO_3F_2)_\infty$. The vibrational modes of the low-temperature polymeric phase, $(OsO_3F_2)_\infty$, have been assigned by comparison with the calculated frequencies of $(\mu\text{-}FOsO_3F_2)_2OsO_3F^-$, providing more complete and reliable assignments than were previously available.

Introduction

Polymeric $(OsO_3F_2)_\infty$ was first synthesized in 1957 by reaction of OsO_4 with BrF_3.[1] Only the melting point and elemental analyses were, however, reported. Three distinct phases of $(OsO_3F_2)_\infty$ were subsequently identified by X-ray powder diffraction: a low-temperature (<90 °C) α-phase (monoclinic), a β-phase (orthorhombic) at intermediate temperatures (90−130 °C), and a γ-phase (orthorhombic) at high temperatures (>130 °C).[2] Single crystals of OsO_3F_2 were obtained by sublimation under static vacuum at 130 °C in a sapphire tube, which resulted in the X-ray crystal structure determination of the low-temperature monoclinic phase (space group $P2_1/c$).[3] The structure consists of an infinite chain in which the pseudo-octahedral Os(VIII) atoms are bridged by fluorine atoms that are trans to oxygen atoms and the three oxygen atoms are in a facial arrangement.

The vibrational characterization of OsO_3F_2 has also been carried out for both the matrix-isolated monomer and $(OsO_3F_2)_\infty$. The infrared[4,5] and Raman[5] spectra of monomeric OsO_3F_2, obtained in both argon and nitrogen matrices at 12 K, are consistent with a trigonal bipyramidal geometry (D_{3h} symmetry) in which the three oxygen atoms lie in the equatorial plane and the fluorine atoms are in axial positions. Although incompletely assigned, the Raman spectra[2,6,7] of solid OsO_3F_2 are consistent

* To whom correspondence should be addressed. E-mail: schrobil@mcmaster.ca.

(1) Hepworth, M. A.; Robinson, P. L. *J. Inorg. Nucl. Chem.* **1957**, *4*, 24–29.
(2) Nghi, N.; Bartlett, N. *C. R. Acad. Sci.* **1969**, *269*, 756–759.
(3) Bougon, R.; Buu, B.; Seppelt, K. *Chem. Ber.* **1993**, *126*, 1331–1336.
(4) Hope, E. G.; Levason, W.; Ogden, J. S. *J. Chem. Soc., Dalton Trans.* **1988**, 61–65.
(5) Beattie, I. R.; Blayden, H. E.; Crocombe, R. A.; Jones, P. J.; Ogden, J. S. *J. Raman Spectrosc.* **1976**, *4*, 313–322.

10.1021/ic900242m CCC: $40.75
Published on Web 04/14/2009

with the low-temperature fluorine-bridged polymeric structure obtained from the single-crystal X-ray structure.[3]

The present paper details the syntheses and structural characterizations by Raman spectroscopy of a new low-temperature phase of OsO_3F_2, namely $(OsO_3F_2)_2$, and its $XeOF_4$ adduct, $(OsO_3F_2)_2{\cdot}2XeOF_4$, which has also been characterized by single-crystal X-ray diffraction. The Raman spectrum of the low-temperature monoclinic α-phase, $(OsO_3F_2)_\infty$, and its assignments are also reported.

Results and Discussion

Syntheses of $(OsO_3F_2)_2{\cdot}2XeOF_4$ and $(OsO_3F_2)_2$. Polymeric OsO_3F_2 slowly dissolved in $XeOF_4$ at room temperature forming a deep orange solution. The ^{19}F NMR spectrum at 30 °C consisted of an exchange-broadened $XeOF_4$ solvent line [$\delta(^{19}F) = 96.0$ ppm, $\Delta\nu_{1/2} = 1800$ Hz] and trace amounts of *cis*-OsO_2F_4 [$\delta(^{19}F) = 68.8$ ppm (t) and 18.5 ppm(t), $^2J(^{19}F-^{19}F) = 138$ Hz)] and XeO_2F_2 [$\delta(^{19}F) = 107.2$ ppm, $\Delta\nu_{1/2} = 521$ Hz]. Fluorine-19 exchange between OsO_3F_2 and $XeOF_4$ solvent not only resulted in broadening of the $XeOF_4$ solvent line but also prevented observation of the fluorine-on-osmium environments of the solute and the ^{129}Xe satellites of the solvent and of XeO_2F_2. The formation of trace amounts of *cis*-OsO_2F_4 and XeO_2F_2 resulted from oxygen/fluorine metathesis between $(OsO_3F_2)_\infty$ and $XeOF_4$ solvent (eq 1).

$$\frac{1}{\infty}(OsO_3F_2)_\infty + XeOF_4 \xrightarrow[30\ ^\circ C]{XeOF_4} OsO_2F_4 + XeO_2F_2 \quad (1)$$

The sample composition was also monitored at intervals by Raman spectroscopy as $XeOF_4$ was removed under dynamic vacuum at 0 °C (Table S1). The Raman spectrum of the initial frozen solution was comprised of bands that arose from a mixture of $XeOF_4$ and $(OsO_3F_2)_2{\cdot}2XeOF_4$. Removal of excess $XeOF_4$ at 0 °C yielded an orange solid corresponding to $(OsO_3F_2)_2{\cdot}2XeOF_4$ (eq 2).

$$\frac{2}{\infty}(OsO_3F_2)_\infty + 2XeOF_4 \xrightarrow[25\ ^\circ C]{XeOF_4} (OsO_3F_2)_2 \cdot 2XeOF_4 \quad (2)$$

Slow cooling of a solution of $(OsO_3F_2)_2{\cdot}2XeOF_4$ in $XeOF_4$ from 25 to 0 °C resulted in light orange needle-shaped crystals of $(OsO_3F_2)_2{\cdot}2XeOF_4$ which were characterized by single-crystal X-ray diffraction (vide infra) and which had a Raman spectrum identical to that of the bulk compound. The $(OsO_3F_2)_2{\cdot}2XeOF_4$ adduct was stable at 25 °C for up to 5 h, after which time dissociation to $(OsO_3F_2)_\infty$ and $XeOF_4$ (eq 3) was detectable by Raman spectroscopy. Upon further

$$(OsO_3F_2)_2 \cdot 2XeOF_4 \xrightarrow{25\ ^\circ C} \frac{2}{\infty}(OsO_3F_2)_\infty + 2XeOF_4 \quad (3)$$

pumping under dynamic vacuum at 0 °C, $(OsO_3F_2)_2{\cdot}2XeOF_4$ slowly lost $XeOF_4$ to give a yellow powder corresponding to $(OsO_3F_2)_2$(eq 4), which was confirmed by Raman spectroscopy (Table S1). Raman spectroscopy established that the dimer was stable indefinitely at 0 °C, but transformed over a period of 2 h at 25 °C to an orange powder corresponding to the monoclinic polymeric phase, $(OsO_3F_2)_\infty$ (eq 5).[2]

$$(OsO_3F_2)_2 \cdot 2XeOF_4 \xrightarrow[0\ ^\circ C]{vac} (OsO_3F_2)_2 + 2XeOF_4 \quad (4)$$

$$\infty(OsO_3F_2)_2 \xrightarrow{25\ ^\circ C} 2(OsO_3F_2)_\infty \quad (5)$$

Table 1. Summary of Crystal Data and Refinement Results for $(OsO_3F_2)_2{\cdot}2XeOF_4$

chem formula	$Os_2O_8F_{12}Xe_2$
space group	$P\bar{1}$ (2)
a (Å)	5.0808(6)
b (Å)	7.7446(9)
c (Å)	9.2133(11)
α (deg)	80.012(4)
β (deg)	83.659(4)
γ (deg)	89.217(4)
V (Å^3)	354.8(1)
molecules/unit cell	1
mol wt (g mol^{-1})	999.00
calcd density (g cm^{-3})	24.675
T (°C)	−173
μ (mm^{-1})	22.76
$R_1{}^a$	0.0408
$wR_2{}^b$	0.0988

[a] R_1 is defined as $\sum||F_o| - |F_c||/\sum|F_o|$ for $I > 2\sigma(I)$. [b] wR_2 is defined as $\{\sum[w(F_o^2 - F_c^2)^2]/\sum w(F_o^2)^2\}^{1/2}$ for $I > 2\sigma(I)$.

X-ray Crystal Structure of $(OsO_3F_2)_2{\cdot}2XeOF_4$. Details of data collection parameters and other crystallographic information are provided in Table 1. Bond lengths and bond angles are listed in Table 2.

The structure consists of $(OsO_3F_2)_2{\cdot}2XeOF_4$ units that are stacked along the *a*-axis but alternate along the *b*- and *c*-axes so that the $XeOF_4$ and OsO_3F_2 molecules face one another in adjacent columns parallel to these axes (Figure S1). The resulting intermolecular contacts are long and are near the sums of the van der Waals radii.[8,9] The OsO_3F_2 molecules are bridged to one another through two fluorine atoms, F(1) and F(1A), that are formally contributed by each OsO_3F_2 molecule. The remaining fluorine ligand of each OsO_3F_2 unit bridges through xenon to a $XeOF_4$ molecule (Figure 1a). The primary coordination spheres of the osmium atoms consist of three oxygen and three fluorine atoms in a facial arrangement, providing a distorted octahedral environment around osmium (Figure 1b). The preference for the *fac*-trioxo structure has been previously discussed for other d^0 transition metal trioxo species such as $(OsO_3F_2)_\infty$,[3] $OsO_3F_3^-$,[10] $[OsO_3F]$-

(6) Falconer, W. E.; Disalvo, F. J.; Griffiths, J. E.; Stevie, F. A.; Sunder, W. A.; Vasile, M. J. *J. Fluorine Chem.* **1975**, *6*, 499–520.
(7) Beattie, I. R.; Livingston, K. M. S.; Reynolds, D. J.; Ozin, G. A. *J. Chem. Soc. A* **1970**, 1210–1216.
(8) Bondi, A. *J. Phys. Chem.* **1964**, *68*, 441–451.
(9) The ranges of long contacts in $(OsO_3F_2)_2{\cdot}2XeOF_4$ are F(6)···F(5A) (2.903(8) Å) to F(1)···F(5B) (3.135(7) Å); F(6)···O(3C) (2.810(8) Å) to F(6)···O(4D) (3.155(8) Å); O(2)···O(4E) (2.954(9) Å) to O(2)···O(3A) (3.168(8) Å); Xe(1)···F(4F) (3.545(6) Å) to Xe(1)···F(5A) (3.684(5) Å); and Xe(1)···O(3C) (3.715(6) Å) to Xe(1)···O(2F) (3.720(6) Å). The corresponding sums of the van der Waals radii (taken from ref 8) are F···F (2.94 Å), F···O (2.99 Å), O···O (3.04 Å), Xe···F (3.63 Å) and Xe···O (3.68 Å).
(10) Gerken, M.; Dixon, D. A.; Schrobilgen, G. J. *Inorg. Chem.* **2000**, *39*, 4244–4255.

Table 2. Experimental and Calculated Geometrical Parameters for $(OsO_3F_2)_2 \cdot 2XeOF_4$ and Calculated Geometrical Parameters for $(OsO_3F_2)_2$, $XeOF_4$, and $(OsO_3F_2)_2 \cdot 2XeOF_4$

$(OsO_3F_2)_2 \cdot 2XeOF_4$					$(OsO_3F_2)_2$		$XeOF_4$	
		calcd (C_i)[b]			calcd (C_{2h})		calcd (C_{4v})	
exptl[a]			SVWN[c]	B3LYP[d]	SVWN[c]	B3LYP[d]	SVWN[c]	B3LYP[e]
			Bond Lengths (Å)					
Os(1)−O(1)	1.703(6)	Os−O_1	1.721	1.688	1.715	1.689		
Os(1)−O(2)	1.684(6)	Os−O_2	1.703	1.683	1.709	1.686		
Os(1)−O(3)	1.685(6)	Os−O_3	1.704	1.683	1.709	1.686		
Os(1)---F(1)	2.117(5)	Os---F_1	2.146	2.147	2.114	2.152		
Os(1)−F(2)	1.927(5)	Os−F_2	1.915	1.921	1.892	1.892		
Os(1)---F(1A)	2.107(4)	Os---F_1'	2.093	2.143	2.114	2.152		
Xe(1)···F(2)	2.757(5)	Xe···F_2	2.735	2.968				
Xe(1)−O(4)	1.709(6)	Xe−O_4	1.750	1.742			1.749	1.742
Xe(1)−F(3)	1.907(5)	Xe−F_3	1.953	1.953			1.951	1.949
Xe(1)−F(4)	1.918(5)	Xe−F_4	1.971	1.953			1.951	1.949
Xe(1)−F(5)	1.912(5)	Xe−F_5	1.949	1.952			1.951	1.949
Xe(1)−F(6)	1.913(5)	Xe−F_6	1.976	1.956			1.951	1.949
Xe(1)···O(1A)	3.983(6)	Xe···O_1'	2.872	3.829				
			Bond Angles (deg)					
O(1)−Os(1)−O(2)	102.0(3)	O_1−Os−O_2	102.7	102.5	102.4	102.2		
O(1)−Os(1)−O(3)	102.1(3)	O_1−Os−O_3	102.7	102.4	102.4	102.2		
O(1)−Os(1)---F(1)	85.3(2)	O_1−Os---F_1	82.2	83.8	82.9	83.0		
O(1)−Os(1)−F(2)	157.4(3)	O_1−Os−F_2	152.9	155.1	152.8	154.2		
O(1)−Os(1)---F(1A)	85.3(2)	O_1−Os---F_1'	83.8	83.8	82.9	83.0		
O(2)−Os(1)−O(3)	105.1(3)	O_2−Os−O_3	105.6	105.3	105.3	105.2		
O(2)−Os(1)---F(1)	159.8(2)	O_2−Os---F_1	162.6	159.8	160.7	160.3		
O(2)−Os(1)−F(2)	91.8(3)	O_2−Os−F_2	94.5	92.5	93.9	93.4		
O(2)−Os(1)---F(1A)	91.5(2)	O_2−Os---F_1'	93.7	92.2	91.4	92.1		
O(3)−Os(1)---F(1)	91.5(3)	O_3−Os---F_1	89.3	91.8	91.4	92.1		
O(3)−Os(1)−F(2)	91.2(3)	O_3−Os−F_2	92.4	92.5	93.9	93.4		
O(3)−Os(1)---F(1A)	159.8(2)	O_3−Os---F_1'	157.4	159.4	160.7	160.3		
F(1)---Os(1)−F(2)	76.1(2)	F_1−Os−F_2	75.6	75.8	75.0	75.8		
F(1)---Os(1)---F(1A)	70.2(2)	F_1−Os---F_1'	70.0	69.2	70.7	69.5		
F(2)−Os(1)---F(1A)	76.5(2)	F_2−Os---F_1'	74.2	75.7	75.0	75.8		
Os(1)---F(1)---Os(1A)	109(1)	Os---F_1---Os′	110.0	110.8	109.3	110.5		
F(2)···Xe(1)···O(1A)	43.2(1)	F_2···Xe···O_1'	55.4	45.4				
F(2)···Xe(1)−F(3)	82.2(2)	F_2···Xe−F_3	105.7	97.2				
F(2)···Xe(1)−F(4)	96.4(2)	F_2···Xe−F_4	69.9	78.3				
F(2)···Xe(1)−F(5)	93.8(2)	F_2···Xe−F_5	70.4	85.3				
F(2)···Xe(1)−F(6)	83.8(2)	F_2···Xe−F_6	105.6	90.1				
F(2)···Xe(1)−O(4)	171.6(2)	F_2···Xe−O_4	154.6	170.3				
O(4)−Xe(1)−F(3)	90.8(3)	O_4−Xe−F_3	92.5	92.2			92.6	92.6
O(4)−Xe(1)−F(4)	90.6(3)	O_4−Xe−F_4	91.8	92.3			92.6	92.6
O(4)−Xe(1)−F(5)	90.8(3)	O_4−Xe−F_5	92.7	92.4			92.6	92.6
O(4)−Xe(1)−F(6)	91.5(3)	O_4−Xe−F_6	91.9	92.3			92.6	92.6
O(4)−Xe(1)···O(1A)	128.5(2)	O_4−Xe···O_1'	149.9	142.7				
F(3)−Xe(1)−F(4)	178.6(2)	F_3−Xe−F_4	175.6	175.5			180	174.8
F(3)−Xe(1)−F(5)	90.0(2)	F_3−Xe−F_5	89.3	90.0			89.9	89.9
F(3)−Xe(1)−F(6)	89.0(2)	F_3−Xe−F_6	89.5	90.1			89.9	89.9
F(3)−Xe(1)···O(1A)	55.6(2)	F_3−Xe···O_1'	68.3	65.6				
F(4)−Xe(1)−F(5)	90.1(2)	F_4−Xe−F_5	89.3	89.9			89.9	89.9
F(4)−Xe(1)−F(6)	90.9(2)	F_4−Xe−F_6	91.6	89.7			89.9	89.9
F(4)−Xe(1)···O(1A)	123.3(2)	F_4−Xe···O_1'	108.2	110.5				
F(5)−Xe(1)−F(6)	177.5(2)	F_5−Xe−F_6	175.3	175.4			180	174.8
F(5)−Xe(1)···O(1A)	122.7(2)	F_5−Xe···O_1'	109.3	116.0				
F(6)−Xe(1)···O(1A)	54.9(2)	F_6−Xe···O_1'	66.0	60.0				
Xe(1)···F(2)−Os(1)	163.2(2)	Xe···F_2−Os	123.2	158.6				
Xe(1)···O(1A)−Os(1)	142.6(3)	Xe···O_1'−Os′	121.0	146.1				

[a] For the atom labeling scheme, see Figure 1a. [b] For the atom labeling scheme, see Figure 6b. [c] SDDall basis set augmented for F, O, and Xe with two d-type polarization functions by Huzinaga.[40] [d] Stuttgart basis set for Os augmented with one f-type polarization functional.[42] aug-cc-pVTZ basis sets for all other atoms. [e] aug-cc-pVTZ basis set.

$[HF][SbF_6]$,[11] ReO_3F,[12] and $ReO_3F(CH_3CN)_2 \cdot CH_3CN$.[13] The occurrence of the bridging fluorine atoms trans to oxygen atoms is also observed in $(OsO_3F_2)_\infty$[3] and other transition metal oxide fluorides, for example, μ-F(*cis*-$OsO_2F_3)_2^+$,[14] polymeric $MO_2F_3 \cdot SbF_5$ (M = Tc, Re),[15] μ-$F(TcOF_4)_2^+$,[16] μ-$F(ReOF_4)_2^+$,[17] μ-F(*cis*-$ReO_2F_3)_2^-$,[13] $Re_3O_6F_{10}^-$,[13] $(WOF_4)_4$,[18] and $(MoOF_4)_\infty$.[19] The *trans*-position of the bridging fluorine ligand is attributed to the *trans*-influence of the doubly bonded oxygen ligand which results from the inability of the fluorine ligand to compete as effectively as an oxygen ligand for the $d_{t_{2g}}$ orbitals of osmium.[20]

(11) Gerken, M.; Dixon, D. A.; Schrobilgen, G. J. *Inorg. Chem.* **2002**, *41*, 259–277.

(12) Supel, J.; Marx, R.; Seppelt, K. *Z. Anorg. Allg. Chem.* **2005**, *631*, 2979–2986.

(13) Casteel, W. J.; Dixon, D. A.; LeBlond, N.; Lock, P. E.; Mercier, H. P. A.; Schrobilgen, G. J. *Inorg. Chem.* **1999**, *38*, 2340–2358.

(14) Casteel, W. J.; Dixon, D. A.; Mercier, H. P. A.; Schrobilgen, G. J. *Inorg. Chem.* **1996**, *35*, 4310–4322.

(15) LeBlond, N.; Dixon, D. A.; Schrobilgen, G. J. *Inorg. Chem.* **2000**, *39*, 2473–2487.

(16) LeBlond, N.; Mercier, H. P. A.; Dixon, D. A.; Schrobilgen, G. J. *Inorg. Chem.* **2000**, *39*, 4494–4509.

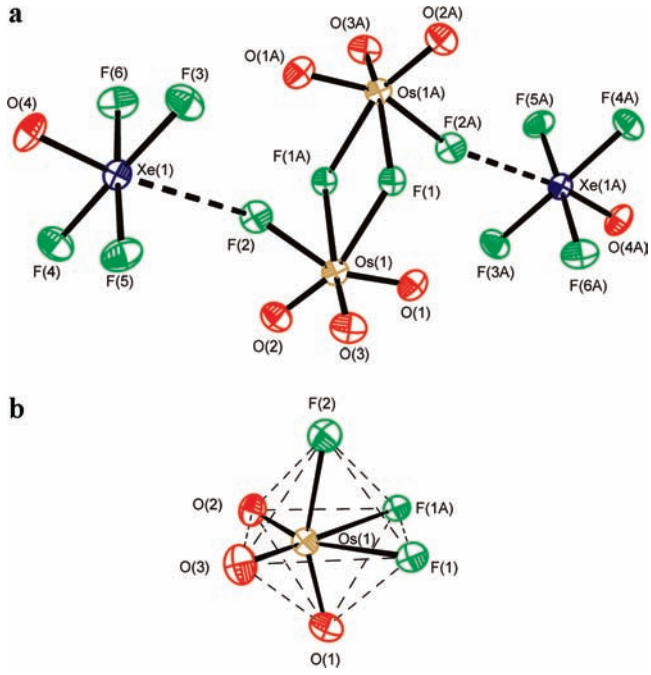

Figure 1. (a) Structural unit in the X-ray crystal structure of $(OsO_3F_2)_2{\cdot}2XeOF_4$ with thermal ellipsoids drawn at the 70% probability level. (b) Visualization of the octahedron formed by the light atoms of the OsO_3F_3 unit.

The Os−O bonds are equal to within $\pm 3\sigma$ and only the Os(1)−O(2,3) bond lengths (1.685(6) Å) are within $\pm 3\sigma$ of those of the polymeric phase (1.688(1) and 1.678(1) Å), whereas the Os(1)−O(1) bond (1.703(6) Å) is significantly shorter than the terminal bond of $(OsO_3F_2)_\infty$ (1.727(1) Å). The fluorine bridges have bond lengths that are equal within $\pm 3\sigma$ (Os(1)---F(1), 2.117(5) Å and Os(1)---F(1A), 2.107(4) Å) and are very similar to those observed for $(OsO_3F_2)_\infty$ (2.126(1) and 2.108(1) Å).[3] The remaining fluorine ligand, F(2), coordinates to Xe(1), forming a Os(1)−F(2)···Xe(1) bridge in which the Xe(1)···F(2) contact (2.757(5) Å) is significantly less than the sum of the van der Waals radii for F and Xe (3.63 Å).[8] The Os(1)−F(2) bond length (1.927(5) Å) is longer than the terminal Os−F bond in the polymeric phase (1.879(1) Å)[3] but is significantly shorter than the Os---F bridge bonds in $(OsO_3F_2)_2$. The Os(1)−F(2) bond length is, in fact, similar to those of the more polar Os−F bonds in the $OsO_3F_3^-$ anion (1.97(1)−1.91(1) Å),[10] and is rendered more basic by the trans influence of the Os(1)−O(1) bond.

The light atoms of $(OsO_3F_2)_2$ form a distorted octahedral coordination sphere about each osmium atom. Although there is significant variation in the bond lengths around the osmium atoms, the light atom octahedra are relatively undistorted (Figure 1b), as shown by the nearest neighbor-ligand atom contacts.[21] The O(1)−Os(1)−F(2) angle (157.4(3)°) is bent away from the Os(1)−O(2,3) double bond domain toward the less repulsive Os(1)---F(1,1A) bridge bonds. The F(1), F(1A), O(2), and O(3) atoms are coplanar within ±0.0001 Å, with the osmium atom lying 0.161 Å out of this plane, and displaced toward O(1). The O(2)−Os(1)−O(3) angle (105.1(3)°) is considerably more open as a result of greater repulsion between the Os−O double bond domains, whereas the F(1)---Os(1)---F(1A) angle (70.2(2)°) is considerably more closed because of weaker repulsions between the longer and more polar Os---F bridge bond domains. The F(1A), F(2), O(1), O(3) [F(1), F(2), O(1), O(2)] atoms are coplanar within ±0.02 [±0.02] Å, and the osmium atom is displaced 0.262 [0.265] Å out of this plane toward O(2) [O(3)]. The displacement of the osmium atom occurs along the pseudo 3-fold axis toward the facial oxygen ligands, which is consistent with the metal atom displacements observed for $(OsO_3F_2)_\infty$,[3] $ReCl_3O_3^{2-}$,[22] and $OsO_3F_3^-$ [10] and for the *cis*-dioxo species *cis*-OsO_2F_4,[23] μ-F(*cis*-$OsO_2F_3)_2^+$,[14] *cis*-$ReO_2F_4^-$,[13] and *cis*-$TcO_2F_4^-$.[20] In the latter cases, the central metal atom (M) is displaced toward the *cis*-oxygen ligands along the axis bisecting the O−M−O angle.

The $XeOF_4$ molecule has been structurally well characterized by ^{19}F NMR,[24] photoelectron,[25] Raman,[26] and gas-phase microwave spectroscopy,[27−29] and by single-crystal X-ray diffraction.[30] Xenon oxide tetrafluoride has been shown to have a square pyramidal geometry based on a AX_4YE VSEPR arrangement, with an axial oxygen atom, four coplanar fluorine atoms in equatorial positions, and an axial valence electron lone pair. The long F(2)···Xe(1) contact in the present structure has no perceptible effect on the geometry of $XeOF_4$ which retains its square-based pyramidal geometry, providing geometric parameters (Table 2) that are in good agreement with those reported previously.[28−30] The only other crystal structure containing the $XeOF_4$ molecule is $[XeF_5][SbF_6]{\cdot}XeOF_4$.[30] The xenon atom of the $XeOF_4$ molecule in this structure has a short Xe···F contact with a fluorine atom of the SbF_6^- anion but has no contacts with the XeF_5^+ cation. This fluorine bridge interaction also does not significantly distort the square-pyramidal geometry of the $XeOF_4$ molecule nor does it result in significant elongation of the Sb−F bridge bond. In the present structure, the

(17) Schrobilgen, G. J.; Holloway, J. H.; Russell, D. R. *J. Chem. Soc., Dalton Trans.* **1984**, 1411–1415.
(18) Edwards, A. J.; Jones, G. R. *J. Chem. Soc. A* **1968**, 2074–2078.
(19) Edwards, A. J.; Steventon, B. R. *J. Chem. Soc. A* **1968**, 2503–2510.
(20) Casteel, W. J.; Dixon, D. A.; LeBlond, N.; Mercier, H. P. A.; Schrobilgen, G. J. *Inorg. Chem.* **1998**, *37*, 340–353.
(21) The interatomic distances for the light atoms forming the coordination spheres of the Os atoms in $(OsO_3F_2)_2{\cdot}2XeOF_4$ are O(1)···O(2,3) 2.634(9), 2.634(9) Å; O(1)···F(1,1A) 2.606(8), 2.600(7) Å; O(2)···O(3) 2.674(8) Å; O(2)···F(1A,2) 2.731(7), 2.599(9) Å; O(3)···F(1,2) 2.740(8), 2.587(8) Å; and F(1A)···F(1,2) 2.428 (9), 2.501(7) Å.
(22) Lis, T. *Acta Crystallogr.* **1983**, *C39*, 961–962.
(23) Christe, K. O.; Dixon, D. A.; Mack, H. G.; Oberhammer, H.; Pagelot, A.; Sanders, J. C. P.; Schrobilgen, G. J. *J. Am. Chem. Soc.* **1993**, *115*, 11279–11284.
(24) Brown, T. H.; Whipple, E. B.; Verdier, P. H. *J. Chem. Phys.* **1963**, *38*, 3029–3030.
(25) Brundle, C. R.; Jones, G. R. *J. Electron Spectrosc. Relat. Phenom.* **1973**, *1*, 403–407.
(26) Tsao, P.; Cobb, C. C.; Claassen, H. H. *J. Chem. Phys.* **1971**, *54*, 5247.
(27) Martins, J.; Wilson, E. B., Jr. *J. Chem. Phys.* **1964**, *41*, 570–571.
(28) Martins, J. F.; Wilson, E. B., Jr. *J. Mol. Spectrosc.* **1968**, *26*, 410–417.
(29) Jacob, E. J.; Thompson, H. B.; Bartell, L. S. *J. Mol. Struct.* **1971**, *8*, 383–394.
(30) Pointner, B. E.; Suontamo, R. J.; Schrobilgen, G. J. *Inorg. Chem.* **2006**, *45*, 1517–1534.

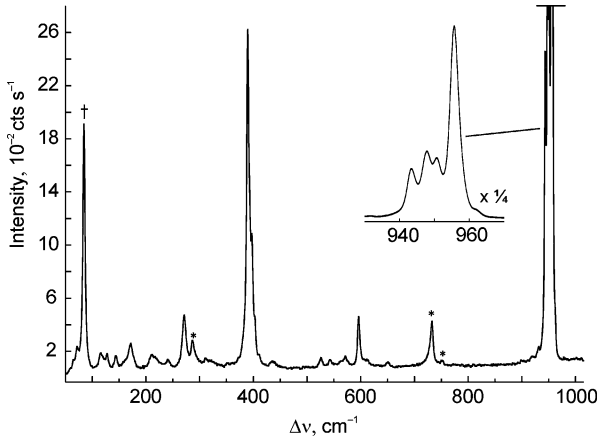

Figure 2. Raman spectrum of $(OsO_3F_2)_\infty$ recorded at −150 °C using 1064-nm excitation; the symbols denote FEP sample tube lines (*) and an instrumental artifact (†).

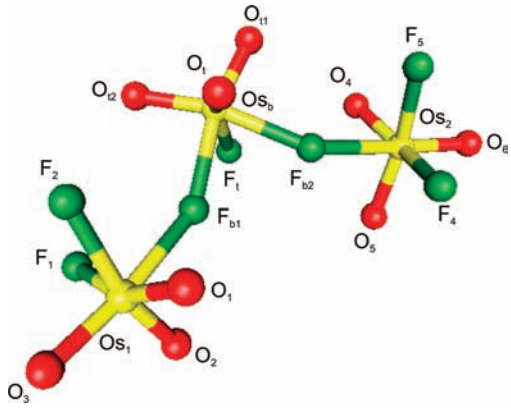

Figure 3. Calculated B3LYP gas-phase geometry for $(\mu\text{-}FOsO_3F_2)_2OsO_3F^-$ (C_1).

primary Xe−F bond lengths range between 1.907(5) and 1.918(5) Å and are equal within $\pm 3\sigma$. The O−Xe−F bond angles are in the range 90.6(3) to 91.5(3)° and are equal within $\pm 3\sigma$, indicating that the repulsive effect of the oxygen double bond domain is comparable to that of the electron lone pair. This is consistent with the crystal structure of $[XeF_5][SbF_6]\cdot XeOF_4$,[30] as well as with gas-phase microwave and electron diffraction studies of $XeOF_4$.[29]

Raman Spectroscopy. The low-temperature, solid-state Raman spectra of $(OsO_3F_2)_\infty$, $(OsO_3F_2)_2$, and $(OsO_3F_2)_2\cdot 2XeOF_4$ are shown in Figures 2, 4, and 5, respectively. The observed and calculated frequencies and assignments for $(OsO_3F_2)_\infty$ and for $(OsO_3F_2)_2$ and $(OsO_3F_2)_2\cdot 2XeOF_4$ are listed in Tables 3 and 4, respectively, where the atom numbering schemes are given in Figures 3, 6a, and 6b, respectively. Spectral assignments for $(OsO_3F_2)_2$ and $(OsO_3F_2)_2\cdot 2XeOF_4$ were made by comparison with the calculated frequencies and Raman intensities (Table 4) for the energy-minimized gas-phase geometries of $(OsO_3F_2)_2$, $XeOF_4$, and $(OsO_3F_2)_2\cdot 2XeOF_4$ and by comparison with the experimental frequencies of $XeOF_4$[26] (Table S2). The vibrational assignments for $(OsO_3F_2)_\infty$ were made by comparison with the calculated frequencies and assignments of the presently unknown $(\mu\text{-}FOsO_3F_2)_2OsO_3F^-$ anion (Table 3 and Table S3). The central OsO_3F_3 group of $(\mu\text{-}FOsO_3F_2)_2OsO_3F^-$ is comprised of two *cis*-bridged fluorine atoms, one terminal fluorine atom, and a *fac*-OsO_3 moiety,

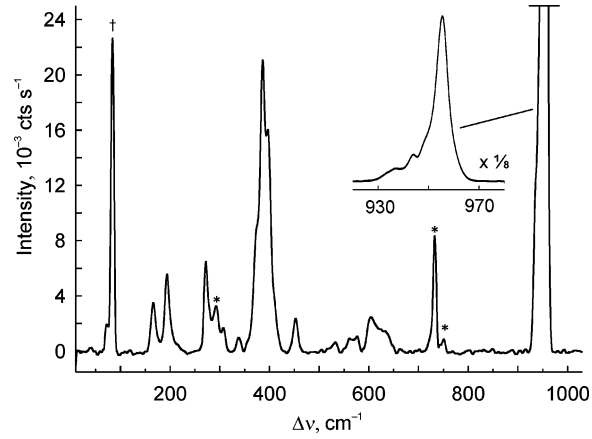

Figure 4. Raman spectrum of $(OsO_3F_2)_2$ recorded at −150 °C using 1064-nm excitation; the symbols denote FEP sample tube lines (*) and an instrumental artifact (†).

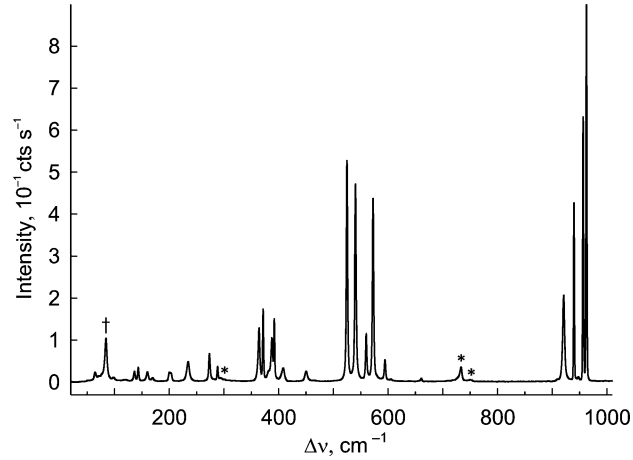

Figure 5. Raman spectrum of $(OsO_3F_2)_2\cdot 2XeOF_4$ recorded at −150 °C using 1064-nm excitation; the symbols denote FEP sample tube lines (*) and an instrumental artifact (†).

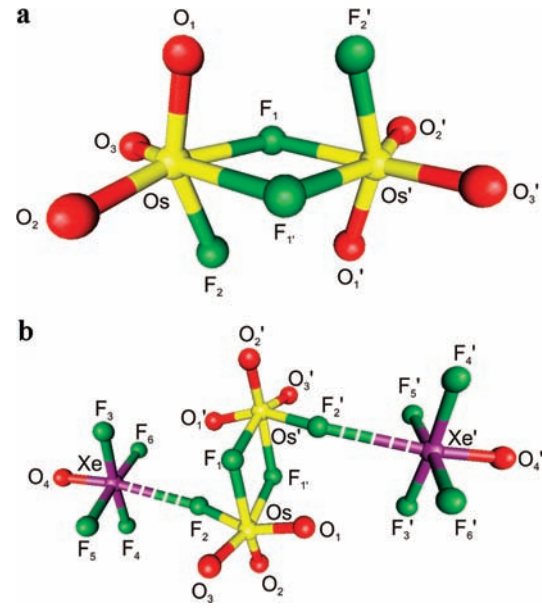

Figure 6. Calculated B3LYP gas-phase geometries for (a) $(OsO_3F_2)_2$ (C_{2h}) and (b) $(OsO_3F_2)_2\cdot 2XeOF_4$ (C_i).

providing a good approximation of the repeat unit in the fluorine-bridged polymer. Moreover, the formal charge of the

Table 3. Raman Frequencies, Intensities, and Assignments for $(OsO_3F_2)_\infty$, and Calculated Vibrational Frequencies and Intensities for $(\mu\text{-}FOsO_3F_2)_2OsO_3F^-$

$(OsO_3F_2)_\infty$			$(\mu\text{-}FOsO_3F_2)_2OsO_3F^-$ (C_1)[d]		
exptl			calcd		assgnts[e]
[a]	[b]	[c]	SVWN	B3LYP	
953(100)	944vs	957(100)	971(158)[44]	1014(97)[39]	$\nu(Os_bO_{t1}) + \nu(Os_bO_{t2}) + \nu(Os_bO_t)$
			970(48)[35]	1008(56)[54]	
			966(2)[97]	1007(72)[67]	
		952(28)	965(10)[217]	994(13)[191]	$\nu(Os_bO_{t1}) - \nu(Os_bO_{t2}) + \nu(Os_bO_t)_{small}$
947(28)		949(33)	964(19)[223]	992(12)[167]	$\nu(Os_bO_{t1}) + \nu(Os_bO_{t2})_{small} - \nu(Os_bO_t)$
			961(86)[108]	985(29)[49]	
			955(27)[39]	983(17)[336]	
			952(21)[15]	980(13)[127]	
941(22)	934mw	945(30)	945(22)[105]	977(10)[69]	$[\nu(Os_bO_t) + \nu(Os_1O_2) + \nu(Os_2O_4)] - [\nu(Os_bO_{t1}) + \nu(Os_1O_1) + \nu(Os_2O_5)]$
748(<1)					
725(<1)					
662(2)					
644(2)	633w	610(2)	652(14)[104]	614(2)[182]	$\nu(Os_bF_t) - [\nu(Os_1F_1) + \nu(Os_1F_2) + \nu(Os_2F_4) + \nu(Os_2F_5)]_{small}$
			628(8)[105]	607(<1)[145]	
596(2)	613mw	596(6)	621(14)[90]	598(17)[7]	$\nu(Os_bF_t) + [\nu(Os_1F_1) + \nu(Os_1F_2) + \nu(Os_2F_4) + \nu(Os_2F_5)]_{small}$
588(2)			567(4)[67]	545(4)[50]	
			560(7)[47]	542(3)[38]	
		413(2)	509(13)[100]	471(5)[73]	$[\nu(Os_bF_{b1}) + \nu(Os_bF_{b2})] - [\nu(Os_1F_{b1}) + \nu(Os_2F_{b2})]$
428(<1) br	449w	404(4)	477(4)[97]	443(<1)[140]	$[\nu(Os_bF_{b1}) + \nu(Os_2F_{b2})] - [\nu(Os_bF_{b2}) + \nu(Os_1F_{b1})]$
			391(13)[3]	416(3)[3]	
			388(7)[2]	415(2)[3]	
	397m	398(10)	381(5)[5]	405(3)[6]	$\delta(Os_bO_tO_{t1}O_{t2})_{oop}$
		394(11)	378(6)[1]	401(7)[7]	$\delta(O_{t1}Os_bO_{t2})$
389(18)	387m	389(29)	373(5)[5]	398(3)[8]	$\delta(O_tOs_bO_{t2}) - \delta(O_tOs_bO_{t1})$
			372(3)[6]	392(7)[4]	
			369(6)[2]	391(7)[3]	
			365(5)[7]	389(2)[27]	
			362(6)[14]	383(2)[36]	
			349(1)[12]	349(<1)[18]	$\rho_w(F_{b1}Os_bF_{b2}) + \delta(F_4Os_2F_5)$
			339(<1)[11]	337(1)[7]	deformation mode
318(<1)		324(2)	314(<1)[13]	336(<1)[9]	$\delta(Os_bF_tF_{b1}F_{b2})_{oop} + \delta(O_1Os_1O_2) - \delta(F_1Os_1F_2)$
		313(1)	310(1)[9]	318(1)[41]	$\rho_w(F_4Os_2O_4) + \rho_w(F_4Os_2\ F_{b2})$
		301(1)	303(1)[18]	306(2)[14]	deformation modes
283(<1)		287(3)	284(5)[15]	293(1)[18]	
271(3)	269w	273(5)	277(4)[11]	282(2)[5]	$\delta(F_tOs_bO_t) + \rho_r(O_1Os_1O_3) + \rho_w(F_1Os_1F_2) + \rho_w(F_4Os_2F_5) + \rho_t(O_6Os_2O_4)$
		262 sh	269(5)[10]	278(2)[9]	deformation modes
			250(1)[10]	267(1)[16]	
		245(1)	237(3)[51]	234(1)[36]	$\rho_t(F_{b2}Os_bF_t) + \rho_t(F_{b1}Os_bF_t) + \rho_r(O_tOs_bO_{t1})$
	235w	223(2)	235(<1)[38]	214(1)[27]	$\delta(F_{b1}Os_bF_{b2}) + \rho_w(F_tOs_bO_t)$
212(2)		214(2)	218(1)[14]	207(<1)[234]	$\rho_t(F_{b1}Os_bF_{b2}) - \rho_t(O_{t1}Os_bO_{t2}) + \delta(O_4Os_2F_4) + \rho_r(O_5Os_2O_6)$
	190w	176(4)	182(1)[3]	168(<1)[2]	deformation modes
		163(1)	169(1)[1]	166(<1)[1]	
	156w	150(2)	147(<1)[3]	155(<1)[20]	
		135(2)	144(<1)[1]	146(<1)[<1]	$\rho_t(O_{t1}Os_bO_{t2}) + \rho_w(O_tOs_bF_t)$
			134(1)[1]	130(<1)[1]	deformation modes
		120(2)	120(<1)[1]	128(<1)[2]	
		91(2)	109(<1)[<1]	110(<1)[3]	
			95(<0.1)[4]	66(<1)[1]	
			84(<0.1)[<1]	44(<1)[<1]	
			81(<0.1)[1]	37(<1)[<1]	
			65(<0.1)[<1]	19(<0.1)[1]	
			52(<1)[<1]	16(<1)[<1]	
			44(<1)[<1]	14(<0.1)[1]	
			39(<1)[1]	7(<0.1)[1]	

[a] From ref 6. [b] From ref 7. The abbreviations denote very strong (vs), medium (m), medium weak (mw), and weak (w) intensities. [c] The Raman spectrum was recorded on a microcrystalline sample in a FEP tube at −150 °C using 1064-nm excitation. The experimental Raman intensities given in parentheses are relative intensities with the most intense band given as 100. The abbreviation, n.o., denotes not observed. [d] SVWN/SDDall. B3LYP/Stuttgart cc-pVTZ. Values in parentheses denote calculated Raman intensities (amu $Å^{-4}$) and values in square brackets denote calculated infrared intensities (km mol^{-1}). [e] Assignments are for the energy-minimized geometry calculated at the B3LYP level; only the mode assignments that involve the central $Os_bO_tO_{t1}O_{t2}F_tF_{b1}F_{b2}$ unit are provided. See Table S3 for a complete set of assignments. See Figure 3 for the atom labeling scheme. The abbreviations denote stretch (ν), bend (δ), umbrella (δ_{umb}), twist (ρ_t), wag (ρ_w), and rock (ρ_r).

Table 4. Calculated and Experimental Vibrational Frequencies, Intensities, and Assignments for $(OsO_3F_2)_2$ and $(OsO_3F_2)_2{\cdot}2XeOF_4$

exptl[a]		calcd[d]				assgnts (C_1)[e]
$(OsO_3F_2)_2$[b]	$(OsO_3F_2)_2{\cdot}2XeOF_4$[c]	$(OsO_3F_2)_2$ (C_{2h})		$(OsO_3F_2)_2{\cdot}2XeOF_4$ (C_i)		$(OsO_3F_2)_2{\cdot}2XeOF_4$
		SVWN	B3LYP	SVWN	B3LYP	
n.o.	n.o.	994(0)[166]	1029(0)[85]	997(0)[100]	1035(0)[73]	$[\nu(OsO_1) + \nu(OsO_2) + \nu(OsO_3)] - [\nu(Os'O_1') + \nu(Os'O_3') + \nu(Os'O_2')]$
955(100)	962(100)	990(114)[0]	1031(116)[0]	1000(162)[0]	1037(114)[0]	$\nu(OsO_1) + \nu(OsO_2) + \nu(OsO_3) + \nu(Os'O_1') + \nu(Os'O_2') + \nu(Os'O_3')$
n.o.	948(1)	986(0)[126]	1018(0)[225]	1003(0)[117]	1025(0)[181]	$[\nu(OsO_2) + \nu(Os'O_3')] - [\nu(OsO_3) + \nu(Os'O_2')]$
948 sh 944(16)	957(39)	986(51)[0]	1010(50)[0]	996(36)[0]	1017(40)[0]	$[\nu(OsO_2) + \nu(Os'O_2')] - [\nu(OsO_3) + \nu(Os'O_3')]$
n.o.	n.o.	979(0)[128]	1007(0)[230]	962(0)[158]	1011(0)[269]	$\nu(OsO_1) - \nu(Os'O_1')$
937(7)	940(47)	972(27)[0]	1001(23)[0]	954(136)[0]	1005(42)[0]	$\nu(OsO_1) + \nu(Os'O_1')$
	921(12)			902(191)[0]	890(74)[0]	$\nu(XeO_4) + \nu(Xe'O_4')$
	911(1)			901(0)[111]	890(0)[77]	$\nu(XeO_4) - \nu(Xe'O_4')$
n.o.		649(0)[130]	632(0)[162]			$\nu(OsF_2) - \nu(Os'F_2')$
	n.o.			616(0)[304]	594(0)[456]	$[\nu(OsF_2) - \nu(Os'F_2')] + [\nu(Xe'F_2') - \nu(XeF_2)]$
604(1) br		630(17)[0]	616(10)[0]			$\nu(OsF_2) + \nu(Os'F_2')$
	n.o.			588(0)[333]	585(0)[472]	$[\nu(XeF_3 + XeF_5) + \nu(Xe'F_4' + Xe'F_6')] - [\nu(XeF_4 + XeF_6) + \nu(Xe'F_3' + Xe'F_5')]$
	594(6)			601(36)[0]	585(6)[0]	$[\nu(XeF_4 + XeF_5) + \nu(Xe'F_4' + Xe'F_5')] - [\nu(XeF_3 + XeF_6) + \nu(Xe'F_3' + Xe'F_6')]$
	n.o.			594(0)[416]	584(0)[366]	$[\nu(XeF_4 + XeF_5) + \nu(Xe'F_3' + Xe'F_6')] - [\nu(XeF_3 + XeF_6) + \nu(Xe'F_4' + Xe'F_5')]$
	560(12)			589(11)[0]	584(1)[0]	$[\nu(XeF_5) + \nu(Xe'F_5')] - [\nu(XeF_6) + \nu(Xe'F_6')]$
	572(48)			579(8)[0]	571(28)[0]	$[\nu(OsF_2) + \nu(Os'F_2')] - [\nu(XeF_2) + \nu(Xe'F_2')]$
	n.o.			536(0)[11]	546(0)[3]	$\nu(XeF_{4e}) - \nu(Xe'F_{4e}')$
	540(51)			536(78)[0]	544(80)[0]	$\nu(XeF_{4e}) + \nu(Xe'F_{4e}')$
	525(58)			506(23)[0]	505(34)[0]	$[\nu(XeF_3 + XeF_4) + \nu(Xe'F_3' + Xe'F_4')] - [\nu(XeF_5 + XeF_6) + \nu(Xe'F_5' + Xe'F_6')]$
	n.o.			508(0)[11]	505(0)[<1]	$[\nu(XeF_3 + XeF_4) + \nu(Xe'F_5' + Xe'F_6')] - [\nu(XeF_5 + XeF_6) + \nu(Xe'F_3' + Xe'F_4')]$
453(1) br	450(3)	450(3)[0]	441(3)[0]	457(3)[0]	447(2)[0]	$\nu(OsF_1) + \nu(Os'F_1) + \nu(Os'F_1') + \nu(OsF_1')$
n.o.	n.o.	394(0)[5]	421(0)[55]	440(0)[44]	420(0)[58]	$\delta(O_1OsF_1) - \delta(O_1'Os'F_1')$
n.o.	n.o.	449(0)[170]	413(0)[109]	396(0)[4]	413(0)[45]	$[\delta(OsO_1O_2O_3) - \delta(Os'O_1'O_2'O_3')] + [\nu(OsF_1) + \nu(OsF_1')] - [\nu(Os'F_1) + \nu(Os'F_1')]$
409(2)	409(4)	376(7)[0]	412(5)[0]	413(8)[0]	413(5)[0]	$[\delta(O_1OsO_2) + \delta(O_1'Os'O_2')] + [\nu(OsF_1) + \nu(Os'F_1')] - [\nu(Os'F_1) + \nu(OsF_1')]$
399 sh 396(9)	392(16)	381(7)[0]	408(6)[0]	380(25)[0]	407(6)[0]	$\delta(OsO_1O_2O_3) + \delta(Os'O_1'O_2'O_3')$
n.o.	n.o.	374(0)[9]	398(0)[3]	378(0)[6]	400(0)[2]	$[\delta(O_1OsO_2) - \delta(O_1'Os'O_2')] + [\delta(O_2'Os'O_3') - \delta(O_2OsO_3)]$
386(13)	388(11)	361(6)[0]	383(5)[0]	377(22)[0]	383(4)[0]	$\delta(O_2OsO_3) + \delta(O_2'Os'O_3')$
376(5)	379(19)	415(1)[0]	374(3)[0]	365(9)[0]	375(4)[0]	$[\nu(OsF_1) + \nu(Os'F_1')] - [\nu(OsF_1') + \nu(Os'F_1)] + \delta(O_3OsF_2) + \delta(O_3'Os'F_2')$
n.o.	381(3)	359(0)[13]	380(0)[39]	364(0)[6]	380(0)[25]	$\delta(O_2OsO_3) - \delta(O_2'Os'O_3')$
337(1)	n.o.	344(0)[10]	353(0)[14]	341(0)[10]	348(0)[16]	$\delta(F_1OsF_2) - \delta(F_1'Os'F_2')$
n.o.	n.o.	355(0)[22]	334(0)[37]	356(0)[19]	337(0)[27]	$[\nu(OsF_1) + \nu(Os'F_1)] - [\nu(OsF_1') + \nu(Os'F_1')]$
	n.o.			308(0)[6]	327(0)[7]	$\delta(O_4XeF_5) - \delta(O_4'Xe'F_5')$
	361 sh 364(14)			311(5)[0]	327(6)[0]	$\delta(O_4XeF_3) + \delta(O_4'Xe'F_3')$
				308(5)[0]	327(5)[0]	$\delta(O_4XeF_5) + \delta(O_4'Xe'F_5')$
	n.o.			310(0)[5]	327(0)[7]	$\delta(O_4XeF_3) - \delta(O_4'Xe'F_3')$

Table 4. Continued

exptl[a]		calcd[d]				assgnts (C_1)[e]
$(OsO_3F_2)_2$[b]	$(OsO_3F_2)_2{\cdot}2XeOF_4$[c]	$(OsO_3F_2)_2$ (C_{2h})		$(OsO_3F_2)_2{\cdot}2XeOF_4$ (C_i)		$(OsO_3F_2)_2{\cdot}2XeOF_4$
		SVWN	B3LYP	SVWN	B3LYP	
308(1)	304(1)	299(<1)[0]	302(<1)[0]	310(3)[0]	300(<1)[0]	$\rho_t(F_1OsF_1')$
n.o.	n.o.	271(0)[5]	284(0)[3]	284(0)[14]	281(0)[2]	$[\rho_t(O_2OsO_3) - \rho_t(O_2'Os'O_3')] + [\rho_w(O_1OsF_2) - \rho_w(O_1'Os'F_2')]$
271(4)	288(4)	278(5)[0]	280(4)[0]	282(5)[0]	277(5)[0]	$\delta(O_1OsF_2) + \delta(O_1'Os'F_2')$
	282(1)			241(0)[128]	263(0)[80]	$\delta_{umb}(XeF_{4e}) - \delta_{umb}(Xe'F_{4e}')$
n.o.	n.o.	243(0)[63]	250(0)[94]	254(0)[42]	243(0)[130]	$\delta(O_1OsF_2) - \delta(O_1'Os'F_2')$
	240 sh 235(5)			249(3)[0]	264(1)[0]	$\delta_{umb}(XeF_{4e}) + \delta_{umb}(Xe'F_{4e}')$
	203(2)			188(3)[0]	209(4)[0]	$\delta(F_4XeF_5) + \delta(F_3XeF_6) + \delta(F_4'Xe'F_5') + \delta(F_3'Xe'F_6')$
	n.o.			187(0)[<1]	209(0)[<0.1]	$[\delta(F_4XeF_5) + \delta(F_3XeF_6)] - [\delta(F_4'Xe'F_5') + \delta(F_3'Xe'F_6')]$
192(3)	201(3)	201(1)[0]	206(1)[0]	199(2)[0]	205(1)[0]	$\rho_t(OsO_1O_2O_3F_2) + \rho_t(Os'O_1'O_2'O_3'F_2')$
166(2)	170(1)	177(1)[0]	172(<1)[0]	205(2)[0]	178(<1)[0]	$[\rho_w(O_1OsF_2) + \rho_w(O_1'Os'F_2')] + \rho_t(F_1OsF_1')$
	n.o.			182(0)[<1]	173(0)[<0.1]	$[\rho_t(F_3XeF_5) + \rho_t(F_3'Xe'F_5')] - [\rho_t(F_4XeF_6) + \rho_t(F_4'Xe'F_6')]$
	160(3)			182(<1)[0]	171(<1)[0]	$[\rho_t(F_3XeF_5) + \rho_t(F_4'Xe'F_6')] - [\rho_t(F_4XeF_6) + \rho_t(F_3'Xe'F_5')]$
	n.o.			132(0)[1]	151(0)[<1]	$[\delta(F_3XeF_5) + \delta(F_4'Xe'F_6')] - [\delta(F_4XeF_6) + \delta(F_3'Xe'F_5')]$
	154 sh			130(1)[0]	151(<1)[0]	$[\delta(F_3XeF_5) + \delta(F_3'Xe'F_5')] - [\delta(F_4XeF_6) + \delta(F_4'Xe'F_6')]$
				142(1)[0]	150(<1)[0]	$[\delta(F_3XeF_6) + \delta(F_3'Xe'F_6')] - [\delta(F_4XeF_5) + \delta(F_4'Xe'F_5')]$
	n.o.			139(0)[2]	150(0)[<1]	$[\delta(F_3XeF_6) + \delta(F_4'Xe'F_5')] - [\delta(F_4XeF_5) + \delta(F_3'Xe'F_6')]$
n.o.	143(4)	140(1)[0]	135(1)[0]	141(2)[0]	136(1)[0]	breathing of $(OsO_3F_2)_2$
n.o.	121(1)	117(0)[<0.1]	117(0)[<1]	153(0)[1]	122(0)[1]	$\rho_t(OsO_2O_3F_2) - \rho_t(Os'O_2'O_3'F_2')$
n.o.	118(1)	109(0)[2]	108(0)[2]	123(0)[4]	109(0)[2]	$\rho_t(OsO_1O_2O_3F_1F_2) - \rho_t(Os'O_1'O_2'O_3'F_1'F_2')$
n.o.	102 sh	92(0)[<0.1]	99(0)[<0.1]	119(0)[<1]	101(0)[<0.1]	$\rho_t(OsO_1O_2O_3) - \rho_t(Os'O_1'O_2'O_3')$
	98(1)	82(<1)[0]	75(<1)[0]	103(4)[0]	74(<1)[0]	$\rho_r(O_2OsO_3) + \rho_r(O_2'Os'O_3')$
	64(2)			106(4)[0]	45(1)[0]	coupled $XeOF_4$ and $(OsO_3F_2)_2$ modes
	n.o.			99(0)[<1]	39(0)[1]	
	n.o.			82(<1)[0]	34(1)[0]	
	n.o.			63(0)[3]	32(0)[1]	
	n.o.			83(1)[0]	26(1)[0]	
	n.o.			78(0)[<1]	26(0)[<1]	
	n.o.			49(<1)[0]	13(<1)[0]	
	n.o.			36(<1)[0]	10(<1)[0]	
	n.o.			30(0)[<0.1]	9(0)[<0.1]	
	n.o.			67(<1)[0]	9(<1)[0]	
	n.o.			48(0)[<1]	8(0)[<1]	
	n.o.			23(0)[<1]	4(0)[<1]	

[a] The Raman spectrum was recorded on a microcrystalline solid sample in a FEP tube at −150 °C using 1064-nm excitation. Experimental Raman intensities are given in parentheses and are relative intensities with the most intense band given as 100. The abbreviations denote shoulder (sh), broad (br), and not observed (n.o.). [b] Bands were also observed at 276(sh), 280(sh), and 288(sh) cm^{-1} but are unassigned. [c] Bands were also observed at 136(3), 274(7), 605(1), and 661(1) cm^{-1} but are unassigned. [d] SVWN/SDDall. Values in parentheses denote calculated Raman intensities (amu $Å^{-4}$) and values in square brackets denote calculated infrared intensities (km mol^{-1}). [e] Assignments are for the energy-minimized geometry calculated at the B3LYP level. See Figure 6a for the atom labeling scheme of $(OsO_3F_2)_2$. See Figure 6b for the atom labeling scheme of $(OsO_3F_2)_2{\cdot}2XeOF_4$. The abbreviations denote stretch (ν), bend (δ), twist (ρ_t), wag (ρ_w), rock (ρ_r), and umbrella (δ_{umb}). The atoms F_3, F_4, F_5, F_6 and F_3', F_4', F_5', F_6' are represented as F_{4e} and F_{4e}', respectively.

anion is evenly dispersed over the light atoms (Table S4) and is not expected to have a significant effect on the vibrational frequencies of the central OsO_3F_3 group.

(a) $(OsO_3F_2)_\infty$. The infrared and Raman spectra of matrix-isolated OsO_3F_2 monomer[4,5] and the Raman spectrum of the low-temperature polymeric phase, $(OsO_3F_2)_\infty$,[6,7] have been previously reported.The vibrational bands of matrix-isolated OsO_3F_2 were fully assigned under D_{3h} symmetry and the $^{16}O/^{18}O$ isotopic shifts for the $Os^{16}O_3F_2$, $Os^{16}O_2{}^{18}OF_2$, $Os^{16}O^{18}O_2F_2$, and $Os^{18}O_3F_2$ isotopomers were used to calculate the principal and the interaction force constants and to confirm the vibrational assignments.[5] Two prior vibrational studies of $(OsO_3F_2)_\infty$[6,7] are at considerable variance with each other and with the present study (Table 3). The Raman spectrum of $(OsO_3F_2)_\infty$ has been re-examined in the present study, providing frequencies and intensities that were reproducible over multiple preparations of $(OsO_3F_2)_\infty$ using different synthetic procedures (see ref 3 and eqs 3 and 5). In addition, more precise descriptions and assignments of the vibrational modes, based on the calculated vibrational frequencies and atomic displacements for $(\mu\text{-}FOsO_3F_2)_2OsO_3F^-$, are also reported. The SVWN and B3LYP frequencies (Table 3) agree well with each other and for the purpose of this discussion, the B3LYP frequencies are explicitly referred to in the subsequent discussion.

Four well-resolved bands occur at 945, 949, 952, and 957 cm^{-1} in the $(OsO_3F_2)_\infty$ spectrum that are assigned to coupled Os_b-O stretching modes. The calculated frequencies associated with the central OsO_3F_3 unit of the $(\mu\text{-}FOsO_3F_2)_2OsO_3F^-$ anion (977, 992, 994, and 1014 cm^{-1}) are overestimated with respect to those of $(OsO_3F_2)_\infty$ but well reproduce the experimental trend. The Os−O stretching frequencies are overestimated by similar amounts for the benchmark, *cis*-OsO_2F_4 (Table S5).

The infinite chain OsO_3F_2 polymer contains two fluorine environments, a terminal (F_t) and a bridging (F_b) environment. The Os_b-F_t stretching bands (596 and 610 cm^{-1}) are weak and are in good agreement with the coupled Os_b-F_t stretching modes calculated for $(\mu\text{-}FOsO_3F_2)_2OsO_3F^-$ (598 and 614 cm^{-1}). The stretching bands involving $Os_b-F_{b(1,2)}$ (404 and 413 cm^{-1}) are also weak, but their frequencies are not modeled as well by $(\mu\text{-}FOsO_3F_2)_2OsO_3F^-$, with the predicted values occurring at much higher frequencies (443 and 471 cm^{-1}, respectively). As anticipated, the Os_b-F_t stretching modes occur at higher frequencies than those involving $Os_b-F_{b(1,2)}$, in accord with the shorter bond length of Os_b-F_t (1.879(1) Å) relative to that of Os_b-F_b (2.126(1) Å).[3]

A limited number of the calculated bending modes (146, 214, 234, 398, 401, and 405 cm^{-1}) are exclusively associated with the central OsO_3F_3 unit and have been explicitly assigned, that is, the bands at 389, 394, and 398 cm^{-1} can be reliably associated with $O-Os_b-O$ bending modes. Detailed descriptions were not attempted for the remaining bending modes because the central OsO_3F_3 and terminal OsO_3F_2 units are extensively coupled. Because $(OsO_3F_2)_\infty$ does not have significant contributions from terminal groups, the highly coupled bending modes of the central OsO_3F_3 and terminal OsO_3F_2 units in $(\mu\text{-}FOsO_3F_2)_2OsO_3F^-$ are inappropriate models for the bending modes in $(OsO_3F_2)_\infty$.

(b) $(OsO_3F_2)_2$ and $(OsO_3F_2)_2{\cdot}2XeOF_4$. Under C_1 symmetry, all vibrational modes (30 A for $(OsO_3F_2)_2$ and 66 A for $(OsO_3F_2)_2{\cdot}2XeOF_4$) are predicted to be both infrared- and Raman-active. Although correlation of the gas-phase adduct symmetry (C_i) to the crystal site symmetry (C_1) results in no additional band splittings, correlation of the site symmetry to the centrosymmetric unit cell symmetry (C_i with $Z = 1$) results in equal apportioning of the vibrational modes between A_g and A_u symmetries (Table S6). Thus, 33 of the 66 A modes of $(OsO_3F_2)_2{\cdot}2XeOF_4$ are Raman-active A_g modes and 33 are infrared-active A_u modes under the unit cell symmetry. In accord with the factor-group analysis, 37 vibrational bands were observed in the Raman spectrum. The calculated frequencies at the SVWN and B3LYP levels are in good agreement with each other. The degree of coupling between the $(OsO_3F_2)_2$ and $XeOF_4$ modes varies with the level of theory, with stronger coupling occurring at the SVWN level. The predominant components in the mode descriptions, however, are the same at both levels and are therefore used as the basis for discussion. The differences arise because the Xe atom of the $XeOF_4$ molecule is coordinated to $F(2)/F_2$ of $(OsO_3F_2)_2$ in both the experimental and B3LYP geometries, while the Xe atom is coordinated to both $F(2)/F_2$ and $O(1A)/O_1'$ of $(OsO_3F_2)_2$ in the SVWN geometry (see Calculated Geometries). Because the B3LYP geometry better reproduces the experimental geometry, the B3LYP frequencies and corresponding mode descriptions are referred to in the following discussion.

The Os−O stretching frequencies of $(OsO_3F_2)_2$ and $(OsO_3F_2)_2{\cdot}2XeOF_4$ (Table 4) are comparable to those of $(OsO_3F_2)_\infty$. The Os−O stretching modes of $(OsO_3F_2)_2{\cdot}2XeOF_4$ are not coupled to any of the $XeOF_4$ modes and are only slightly shifted to higher frequency relative to those of $(OsO_3F_2)_2$.

The $Os-F_{(2,2')}$ and $Xe-F_{(2,2')}$ stretching modes of the fluorine bridge are coupled, giving rise to two modes, $([\nu(OsF_2) - \nu(Os'F_2')] + [\nu(Xe'F_2') - \nu(XeF_2)])$ and $([\nu(OsF_2) + \nu(Os'F_2')] - [\nu(Xe'F_2') + \nu(XeF_2)])$. Only the latter mode is observed at 572 cm^{-1} as a strong band, which is in good agreement with the calculated frequency (571 cm^{-1}) and strong intensity. The frequency of this mode is shifted to lower frequency when compared with that of the $[\nu(OsF_2) + \nu(Os'F_2')]$ mode in $(OsO_3F_2)_2$, observed at 604 cm^{-1} as a broad, low-intensity band. The experimental frequency difference upon going from the dimer to the adduct (32 cm^{-1}) is in reasonable agreement with the calculated shift (45 cm^{-1}). A similar shift (38 cm^{-1}) was calculated for the modes involving $[\nu(OsF_2) - \nu(Os'F_2')]$.

In contrast, and as expected, all stretching mode descriptions and frequencies that involve $Os-F_{(1,1')}$ are nearly identical for both $(OsO_3F_2)_2$ and $(OsO_3F_2)_2{\cdot}2XeOF_4$. The in-phase mode, $[\nu(OsF_1) + \nu(Os'F_1) + \nu(Os'F_1') + \nu(OsF_1')]$, appears as a weak band at 453 and 450 cm^{-1}, respectively.

The out-of-phase mode, $[\nu(OsF_1) + \nu(Os'F_1')] - [\nu(Os'F_1) + \nu(OsF_1')]$, is significantly coupled with bending modes, giving rise to bands at 376 and 409 cm^{-1} for the dimer and at 379 and 409 cm^{-1} for the adduct. The frequency at 409 cm^{-1} is in very good agreement with the Os_b-F_b frequencies of $(OsO_3F_2)_\infty$ (404, 413 cm^{-1}).

Most of the O−Os−O, F−Os−O, and F−Os−F bending modes are not coupled or are very weakly coupled to the F−Xe−F and F−Xe−O bending modes of the $(OsO_3F_2)_2{\cdot}2XeOF_4$ adduct and are generally in very good agreement with the calculated values, as well as with the experimental and calculated values for $(OsO_3F_2)_2$ and $(OsO_3F_2)_\infty$.

The $XeOF_4$ molecules adducted to $(OsO_3F_2)_2$ are rendered non-equivalent because the C_i site symmetry of the adduct results in lowering of the free molecule symmetry from C_{4v} to local C_1 symmetry and removal of the degeneracies of the E vibrational modes. In addition, all $XeOF_4$ vibrational modes are coupled to each other but, for the most part, do not exhibit significant coupling with the $(OsO_3F_2)_2$ modes, except in the case noted above.

Both the symmetric (921 cm^{-1}) and asymmetric (911 cm^{-1}) Xe−O stretching modes of $(OsO_3F_2)_2{\cdot}2XeOF_4$ occur at higher frequencies than the calculated values (890 and 890 cm^{-1}, respectively, Table 4). The Xe−O stretching modes are shifted to lower frequency than that of the experimental and calculated gas-phase $XeOF_4$ molecule[26] (927 and 928 cm^{-1}, respectively, Table S2), in accordance with coordination of the Lewis acidic $XeOF_4$ molecule.

Computational Results. The geometries of $(OsO_3F_2)_2$ and $(OsO_3F_2)_2{\cdot}2XeOF_4$ (Figure 6) optimized under C_{2h} and C_i symmetries, respectively, and resulted in stationary points with all frequencies real. The starting geometries for both energy minimizations were the crystallographic geometries. Although $(OsO_3F_2)_2$ optimized to C_{2h} symmetry, the geometry is very close to C_i symmetry, which is reflected in the atom labeling scheme used in Figure 6a. The energy-minimized geometries and vibrational frequencies of the benchmarks, $XeOF_4$ (C_{4v}) and *cis*-OsO_2F_4 (C_{2v}) (Tables S2 and S5, respectively) were also calculated. The geometry of the $XeOF_4$ molecule has been energy minimized using the SVWN/SDDall and B3LYP/aug-cc-pVTZ methods and provides geometrical parameters and frequencies that are similar to the experimental values of $XeOF_4$[26] and $(OsO_3F_2)_2{\cdot}2XeOF_4$.

The energy-minimized geometry of the presently unknown $(\mu\text{-}FOsO_3F_2)_2OsO_3F^-$ anion was obtained for C_1 symmetry (Table S7), resulting in a stationary point with all frequencies real. Descriptions of the vibrational modes are provided in Table S3. The vibrational modes and frequencies of the $(\mu\text{-}FOsO_3F_2)_2OsO_3F^-$ anion were used to aid the vibrational assignments of the infinite-chain polymer, $(OsO_3F_2)_\infty$. The central OsO_3F_3 group of the anion provided a satisfactory model for the OsO_3F_3 group of the polymer. Moreover, the formal negative charge of the anion is essentially equally distributed among all of the electronegative light atoms (see Table S4) so that the formal negative charge may be expected to have a minimal effect on the geometrical parameters and vibrational frequencies associated with the OsO_3F_3 group.

(a) Calculated Geometries. (i) $(OsO_3F_2)_2$ and $(OsO_3F_2)_2{\cdot}2XeOF_4$. The energy-minimized geometries calculated at the SVWN/SDDall (Figure S2) and B3LYP/Stuttgart(Os) aug-cc-pVTZ (Xe, O, F) levels (Figure 6b) for $(OsO_3F_2)_2{\cdot}2XeOF_4$ only differ by the relative positions of the $XeOF_4$ molecules in relation to the $(OsO_3F_2)_2$ dimer, with the B3LYP geometry more closely reproducing the experimental interaction between $(OsO_3F_2)_2$ and $XeOF_4$. The experimental (2.757(5) Å) and SVWN (2.735 Å) Xe···F_2 bond lengths are in close agreement, whereas the B3LYP bond length is slightly longer (2.968 Å). In contrast, the B3LYP (3.829 Å) and SVWN (2.872 Å) Xe···O_1' contact distances are both shorter than the experimental distance (3.983(6) Å). The Xe atom of the $XeOF_4$ molecule is nearly equidistant from O_1' and F_2 at the SVWN level, whereas it is much closer to $F(2)/F_2$ for the experimental and B3LYP geometries. The Xe···$F(2)/F_2$−Os bond angles for the experimental (163.2(2)°), B3LYP (158.6°), and SVWN (123.2°) geometries also reflect the shorter Xe···$F(2)/F_2$ distance.

The calculated $(OsO_3F_2)_2$ and $(OsO_3F_2)_2{\cdot}2XeOF_4$ geometries are in good agreement with the experimental geometry of the dimer unit in $(OsO_3F_2)_2{\cdot}2XeOF_4$, although the Os−O bond lengths are slightly overestimated in the calculated structures. Both calculated structures provide good estimates for the Os---F_1 bond lengths whereas the calculated Os−F_2 bond length of $(OsO_3F_2)_2$ is underestimated when compared with the experimental and calculated values for $(OsO_3F_2)_2{\cdot}2XeOF_4$. This is likely attributable to the significant interaction that occurs between F_2 and Xe in $(OsO_3F_2)_2{\cdot}2XeOF_4$. The Os−$O_1$ and Os′−O_1' bond lengths of $(OsO_3F_2)_2{\cdot}2XeOF_4$ calculated at the SVWN level (1.721 Å) are longer than the B3LYP (1.688 Å) and experimental (1.703(6) Å) values because of the much shorter $O_{1,1}'$···Xe(′) contacts in the SVWN geometry. The absence of an interaction between O_1 and Xe in the experimental structure is also consistent with the similar calculated and experimental Os−O_1 bond lengths found for $(OsO_3F_2)_2$.

In both the calculated and experimental structures of $(OsO_3F_2)_2$ and $(OsO_3F_2)_2{\cdot}2XeOF_4$, the light atoms of the $(OsO_3F_2)_2$ dimer lie in two dihedral planes; one composed of atoms $O_2,O_3,Os,F_1,F_1',Os',O_2',O_3'$, and the other composed of atoms F_2,Os,O_1,O_1',Os',F_2'. In the case of the O_1−Os−F_2 and O_1'−Os′−F_2' bond angles, both are bent toward the fluorine bridge atoms, F_1 and F_1' (Figure 6).

The shorter $O_{1,1}'$···Xe(′) bond length obtained for the SVWN geometry results in a O_4−Xe···F_2 bond angle that is more closed than in the B3LYP and experimental geometries (154.6, 170.3, and 171.6(2)°, respectively). In both the SVWN and B3LYP geometries, the O_4−Xe···O_1' bond angle is calculated to be larger than in the experimental structure (149.9, 142.7, and 128.5(2)°, respectively), with the difference likely due to crystal packing. In the geometry calculated at the SVWN level, the Xe atom is essentially equidistant from the F_2 atom and the O_1' atom, while in the

B3LYP geometry, the Xe atom lies along a line coincident with the Os−F_2 bond that has no significant interaction with O_1', in agreement with the crystal structure. In both calculated structures, the Xe−F and Xe−O bond lengths of the $XeOF_4$ molecule are slightly overestimated and the angle formed between O_4 and the plane defined by the F_3, F_4, F_5, F_6 atoms is also slightly overestimated.

(ii) (μ-$FOsO_3F_2)_2OsO_3F^-$. The structure of the (μ-$FOsO_3F_2)_2OsO_3F^-$ anion, optimized at the B3LYP (Figure 3) and SVWN (values in square brackets) levels (Table S7), has both terminal OsO_3F_2 units orientated so that the $Os_1-F_{b1}-Os_b-F_{b2}-Os_2$ backbone forms a shallow W-shaped arrangement. The $Os_1\text{---}F_{b1}\text{---}Os_b$ (144.7 [129.8]) and $Os_2\text{---}F_{b2}\text{---}Os_b$ (144.4° [128.8]) bridge bond angles are bent away from each other, as a result, $\angle Os_1Os_bOs_2$ is significantly greater than 90° (106.5° [116.4]).

The $Os_1\text{---}F_{b1}$ and $Os_2\text{---}F_{b2}$ bridge bond lengths of the terminal OsO_3F_3 units (av., 2.194 Å) are elongated with respect to the terminal $Os_{(1,2)}-F$ bond lengths (av., 1.922 Å). The bridging $Os_b\text{---}F_{b1}$ and $Os_b\text{---}F_{b2}$ bond lengths (av., 2.072 Å) and the terminal Os_b-F_t bond (1.904 Å) are shorter than the respective bridging $Os_{1,2}\text{---}F_b$ and terminal $Os_{1,2}-F_{1,2,4,5}$ bond lengths. In contrast with the experimental Os−O bond lengths of $(OsO_3F_2)_\infty$ (1.727(1), 1.688(1), and 1.678(1) Å),[3] the calculated $Os_b-O_{(t,t1,t2)}$ bond lengths of (μ-$FOsO_3F_2)_2OsO_3F^-$ are nearly equal and are not significantly influenced by the *trans*-fluorine ligands. It is noteworthy that the *trans*-influence on the Os−O bond lengths is observed for the experimental structure of $(OsO_3F_2)_2{\cdot}2XeOF_4$ but was not apparent in the calculated structures of $(OsO_3F_2)_2$ and $(OsO_3F_2)_2{\cdot}2XeOF_4$.

(b) Charges, Valencies, and Bond Orders. The Natural Bond Orbital (NBO)[31−34] analyses were carried out for the SVWN- and B3LYP-optimized gas-phase geometries of $(OsO_3F_2)_2$ and $(OsO_3F_2)_2{\cdot}2XeOF_4$ and are similar (Table S8). Because the B3LYP geometry better reproduces the experimental geometry than the SVWN geometry (see Calculated Geometries), only the B3LYP results are referred to in the ensuing discussion.

The NBO analyses give natural charges of 2.19 and 2.18 for Os in $(OsO_3F_2)_2$ and $(OsO_3F_2)_2{\cdot}2XeOF_4$, respectively, and 3.13 for Xe in $(OsO_3F_2)_2{\cdot}2XeOF_4$. The natural charge of the Xe atom is approximately half of its formal oxidation number, and the oxygen and fluorine atoms are also close to half of their respective formal oxidation numbers, indicating that the bonding in $(OsO_3F_2)_2$ and $(OsO_3F_2)_2{\cdot}2XeOF_4$ is, as expected, polar covalent. The $Os\text{---}F_1$ bridge bond order (0.23, 0.23) is approximately half that of the terminal Os−F_2 bond (0.43, 0.40) for both $(OsO_3F_2)_2$ and $(OsO_3F_2)_2{\cdot}2XeOF_4$, respectively, which is consistent with equivalent bonding of the F_1 bridging fluorine atom to both osmium atoms.

With the exception of F_2, the Os−O and Os−F bond orders of $(OsO_3F_2)_2$ and $(OsO_3F_2)_2{\cdot}2XeOF_4$ are comparable. The Os−F_2 bond order for $(OsO_3F_2)_2{\cdot}2XeOF_4$ (0.40) is slightly lower when compared with that of $(OsO_3F_2)_2$ (0.43) and is attributable to coordination of F_2 to the Xe atom of $XeOF_4$. The Xe···F_2 bond order corresponding to this weak fluorine bridge interaction is only 0.04.

Conclusions

The $(OsO_3F_2)_2{\cdot}2XeOF_4$ adduct has been synthesized by reaction of $(OsO_3F_2)_\infty$ with $XeOF_4$ solvent and is composed of the doubly fluorine bridged $(OsO_3F_2)_2$ dimer and two $XeOF_4$ molecules which interact with the terminal fluorine ligands of the dimer by means of fluorine bridges between the Xe(VI) and Os(VIII) atoms. The $XeOF_4$ molecule retains its square pyramidal geometry, and the primary coordination spheres of the osmium atoms are *fac*-OsO_3F_3 arrangements in which the oxygen ligands are cis to one another and the bridging fluorine atoms are trans to an oxygen ligand. The adduct is stable at room temperature for up to 5 h, slowly dissociating to $(OsO_3F_2)_\infty$ and $XeOF_4$. The $(OsO_3F_2)_2$ dimer has been isolated by removal of $XeOF_4$ from $(OsO_3F_2)_2{\cdot}2XeOF_4$ under dynamic vacuum and represents a new low-temperature phase of OsO_3F_2. Upon standing at 25 °C, the dimer undergoes an irreversible phase transition to the α-phase of $(OsO_3F_2)_\infty$, a polymeric chain structure. The vibrational modes and the Raman spectrum of $(OsO_3F_2)_\infty$ have been assigned in detail with the aid of quantum-chemical calculations of the presently unknown trinuclear (μ-$FOsO_3F_2)_2OsO_3F^-$ anion. Because the negative formal charge was found to be essentially uniformly dispersed over all the light atoms, the vibrational modes of the central OsO_3F_3 moiety of this anion proved to be a good model for the assignment of the vibrational modes of the OsO_3F_3 moieties in the infinite chain polymer, $(OsO_3F_2)_\infty$.

Experimental Section

Apparatus and Materials. Manipulations involving air-sensitive materials were carried out under anhydrous conditions as previously described.[14] All preparative work was carried out in fluoroplastic vessels fabricated from $^1/_4$-in. o.d. lengths of FEP tubing. The tubing was heat-sealed at one end and connected through a 45° SAE flare to a Kel-F valve. Reaction vessels were dried on a glass vacuum line and then transferred to a metal vacuum line where they were passivated with F_2 for several hours, refilled with dry N_2, and stored in a drybox until used. Vessels were connected to vacuum lines through $^1/_4$-in. 316 stainless steel Swagelok Ultratorr unions fitted with Viton O-rings. Xenon oxide tetrafluoride was synthesized by hydrolysis of XeF_6 as previously described[35] and $(OsO_3F_2)_\infty$ was synthesized by reaction of OsO_4 (Koch-Light, 99.9%) with ClF_3 as previously described.[3]

Syntheses of $(OsO_3F_2)_2{\cdot}2XeOF_4$ and $(OsO_3F_2)_2$. Inside a nitrogen-filled drybox, a fluorine passivated FEP reaction vessel

(31) Glendening, E. D.; Reed, A. E.; Carpenter, J. E.; Weinhold, F. *NBO*, Version 3.1; Gaussian Inc.: Pittsburgh, PA, 1990.
(32) Reed, A. E.; Curtiss, L. A.; Weinhold, F. *Chem. Rev* **1998**, *88*, 899–926.
(33) Reed, A. E.; Weinstock, R. B.; Weinhold, F. *J. Chem. Phys.* **1985**, *83*, 735–746.
(34) Glendening, E. D.; Badenhoop, J. K.; Reed, A. E.; Carpenter, J. E.; Bohmann, C. M.; Morales, C. M.; Weinhold, F. *NBO Version 5.0*; Theoretical Chemical Institute, University of Wisconsin: Madison, WI, 2001.
(35) Schumacher, G. A.; Schrobilgen, G. J. *Inorg. Chem.* **1984**, *23*, 2923–2929.

was loaded with 0.02803 g (0.1015 mmol) of orange $(OsO_3F_2)_\infty$. The reaction vessel was then transferred to a metal vacuum line and about 1.0 g (4.5 mmol) of $XeOF_4$ was distilled into it. Upon warming to room temperature, an orange suspension formed which slowly dissolved, with agitation, over a period of several hours to form a deep orange solution. The reaction vessel was attached to a metal vacuum line through a FEP U-trap cooled to −196 °C and excess $XeOF_4$ was removed under dynamic vacuum at 0 °C. Pumping for about $2^1/_2$ min yielded an orange solid that was identified as $(OsO_3F_2)_2 \cdot 2XeOF_4$ (0.04931 g, 0.04936 mmol) by Raman spectroscopy. Associated $XeOF_4$ was removed from the adduct by further pumping on the solid at 0 °C for 3 h, producing a yellow powder identified as $(OsO_3F_2)_2$ (0.02720 g, 0.04924 mmol) by Raman spectroscopy. The dimer underwent a phase transition to $(OsO_3F_2)_\infty$ when warmed to and maintained at room temperature for $1^1/_2$ h, whereas the Raman spectrum of the $XeOF_4$ adduct showed no change when the sample was held at room temperature for up to 5 h. Slow dissociation of $XeOF_4$ and rearrangement of $(OsO_3F_2)_2$ to $(OsO_3F_2)_\infty$ was, however, detected upon further standing at room temperature and was complete after 21 days.

Raman Spectroscopy. The low-temperature Raman spectra of $(OsO_3F_2)_\infty$, $(OsO_3F_2)_2 \cdot 2XeOF_4$, $XeOF_4$, and $(OsO_3F_2)_2$ (−150 °C) were recorded on a Bruker RFS 100 FT Raman spectrometer using 1064-nm excitation and a resolution of 1 cm^{-1} as previously described.[10] The spectrum was recorded using a laser power of 300 mW and a total of 1200 scans for $(OsO_3F_2)_\infty$, $(OsO_3F_2)_2 \cdot 2XeOF_4$, and $XeOF_4$ and 2400 scans for $(OsO_3F_2)_2$.

Nuclear Magnetic Resonance Spectroscopy. (a) NMR Sample Preparation. In a typical synthesis, a sample of $(OsO_3F_2)_2 \cdot 2XeOF_4$ was prepared in a 4-mm o.d. FEP tube fitted with a Kel-F valve that had been loaded with $(OsO_3F_2)_\infty$ (23.24 mg, 0.08314 mmol) inside a drybox. The NMR tube was connected to a FEP vacuum submanifold that was, in turn, connected to a $XeOF_4$ storage vessel. The FEP submanifold was connected to a metal vacuum line, and about 0.5 mL of $XeOF_4$ was statically distilled onto $(OsO_3F_2)_\infty$ at −196 °C. The NMR sample was then heat sealed under dynamic vacuum and stored at −196 °C until its ^{19}F NMR spectrum could be recorded. Samples were dissolved at room temperature just prior to data acquisition. When obtaining spectra, the 4-mm FEP tubes were inserted into a 5-mm o.d. thin-wall precision glass NMR tube (Wilmad).

(b) NMR Instrumentation and Spectral Acquisitions. Fluorine-19 NMR spectra were recorded unlocked (field drift <0.1 Hz h^{-1}) on a Bruker DRX-500 spectrometer equipped with an 11.744 T cryomagnet using a 5 mm combination $^1H/^{19}F$ probe operating at 470.592 MHz. The NMR probe was cooled using a nitrogen flow and variable-temperature controller (BVT 3000).

The ^{19}F NMR spectra were acquired in 32 K memories with spectral width settings of 37.5 kHz and acquisition times of 0.87 s, and were zero-filled to 64 K, yielding data point resolutions of 0.57 Hz/data point. Relaxation delays of 0.1 s were applied and 2500 transients were accumulated. The pulse width, corresponding to a bulk magnetization tip angle of approximately 90°, was 8.5 μs. Line broadenings of 0.1 Hz were used in the exponential multiplications of the free induction decays prior to Fourier transformation. The ^{19}F spectra were referenced externally at 30 °C to samples of neat $CFCl_3$. The chemical shift convention used is that a positive (negative) sign indicates a chemical shift to high (low) frequency of the reference compound.

X-ray Crystal Structure Determination of $(OsO_3F_2)_2 \cdot 2XeOF_4$. (a) Crystal Growth. Crystals of $(OsO_3F_2)_2 \cdot 2XeOF_4$ were obtained from a sample composed of 0.0502 g (0.182 mmol) of OsO_3F_2 dissolved in excess $XeOF_4$ (ca. 0.500 g, 2.24 mmol) and contained in a $^1/_4$-in. o.d. FEP T-shaped reactor. The sample vessel was placed in a near-horizontal position, distributing the $XeOF_4$ solution along the length of the reaction vessel. Slow cooling of the solution to 0 °C over 3 h resulted in the growth of light orange needles while the supernatant remained deep orange in color. Crystals were isolated by decanting the solvent at −5 °C under dry nitrogen into the side arm of the FEP vessel, which was immersed in liquid nitrogen, followed by drying of the crystalline product under dynamic vacuum at −20 °C before the side arm containing the supernatant was removed by heat sealing off this portion of the reaction vessel under dynamic vacuum at −196 °C.

(b) Collection and Reduction of X-ray Data. A crystal of $(OsO_3F_2)_2 \cdot 2XeOF_4$ having the dimensions 0.17 × 0.04 × 0.03 mm^3 was selected at −105 ± 3 °C for low-temperature X-ray structure determination and was mounted in a cold stream (−173 °C) on a goniometer head as previously described.[10]

The crystal was centered on a Bruker SMART APEX II diffractometer, equipped with an APEX II 4K CCD area detector and a triple-axis goniometer, controlled by the APEX2 Graphical User Interface (GUI) software,[36] and a sealed source emitting graphite-monochromated Mo Kα radiation (λ = 0.71073 Å). Diffraction data collection at −173 °C consisted of a full φ rotation at a fixed $\chi = 54.74°$ with 0.36° (1010) frames, followed by a series of short (250 frames) ω scans at various φ settings to fill the gaps. The crystal-to-detector distance was 4.953 cm and the data collection was carried out in a 512 × 512 pixel mode using 2 × 2 pixel binning. Processing of the raw data was completed by using the APEX2 GUI software,[36] which applied Lorentz and polarization corrections to three-dimensionally integrated diffraction spots. The program SADABS[37] was used for the scaling of diffraction data, the application of a decay correction, and an empirical absorption correction on the basis of the intensity ratios of redundant reflections.

(c) Solution and Refinement of the Structure. The XPREP program was used to confirm the unit cell dimensions and the crystal lattice. The solution was obtained by direct methods which located the positions of the atoms defining the $(OsO_3F_2)_2$ dimer and the $XeOF_4$ molecules. The final refinement was obtained by introducing anisotropic thermal parameters and the recommended weightings for all of the atoms. The maximum electron densities in the final difference Fourier map were located near the heavy atoms. All calculations were performed using the SHELXTL-plus package for the structure determination and solution refinement and for the molecular graphics.[38] Further confirmation of the choice of space group was obtained by use of PLATON with the WinGX software package.[39]

Computational Methods. The optimized geometries and frequencies of OsO_3F_2, *cis*-OsO_2F_4, $XeOF_4$, $(OsO_3F_2)_2$, $(OsO_3F_2)_2 \cdot 2XeOF_4$, and $(\mu\text{-}FOsO_3F_2)_2OsO_3F^-$ were calculated at the density functional theory (DFT) level by use of SVWN and B3LYP[40] methods. The Stuttgart semirelativistic large core and effective core pseudopotential basis sets (SDDall) augmented for F, O, and Xe with two d-type polarization functions by Huzinaga[41] was used for

(36) *APEX2*, Release 2.0−2; Bruker AXS Inc.: Madison, WI, 2005.
(37) Sheldrick, G. M. *SADABS (Siemens Area Detector Absorption Corrections)*, version 2.10; Siemens Analytical X-ray Instruments Inc: Madison, WI, 2004.
(38) Sheldrick, G. M., *SHELXTL-Plus, release 6.14, Siemens Analytical X-ray Instruments, Inc*; Madison, WI, 2000−2003.
(39) Farrugia, L. J. *J. Appl. Crystallogr.* **1999**, *32*, 837–838.
(40) Frisch, M. J. et al. *Gaussian 03*, revision B.04; Gaussian, Inc.: Pittsburgh, PA, 2003.
(41) Huzinaga, S.; Andzelm, J.; Kolobukowski, M.; Radzio-Andzelm, E.; Sakai, Y.; Tatewaki, H. *Gaussian Basis Sets for Molecular Calculations*; Physical Science Data 16; Elsevier: Amsterdam, 1984.

the SVWN method and the Stuttgart basis set augmented by one f-type polarization function (α_f Os 0.886)[42] for osmium and aug-cc-pVTZ basis sets for xenon, oxygen, and fluorine was used for the B3LYP method.

Pseudopotentials were used with the appropriate basis sets for both osmium and xenon. Quantum-chemical calculations were carried out using the programs Gaussian 98 and Gaussian 03.[43] The levels and basis sets were benchmarked by calculating *cis*-OsO_2F_4 and $XeOF_4$ and comparing with the experimental geometries and vibrational frequencies.[23,29,30] The geometries were fully optimized using analytical gradient methods. After optimization at one level of theory, the geometries were calculated at the other level of theory to ensure an equivalent energy-minimized geometry had been achieved. The vibrational frequencies were calculated at the SVWN and B3LYP levels using the appropriate minimized structure, and the vibrational mode descriptions were assigned with the aid of Gaussview.[44]

Acknowledgment. We thank the Natural Sciences and Engineering Research Council of Canada for the award of a postgraduate scholarship (M.J.H.) and for support in the form of a Discovery Grant (G.J.S.); and SHARCNet (Shared Hierarchical Academic Research Computing Network; www.sharcnet.ca) for computational resources.

Supporting Information Available: Raman spectra used to monitor the formation/dissociation of $(OsO_3F_2)\cdot 2XeOF_4$ from/to $(OsO_3F_2)_\infty$ and $XeOF_4$, and the transition of $(OsO_3F_2)_2$ to $(OsO_3F_2)_\infty$ (Table S1); view of the $(OsO_3F_2)_2\cdot 2XeOF_4$ crystallographic unit cell along the *a*-axis. (Figure S1); experimental Raman frequencies, intensities, and assignments for gas-phase $XeOF_4$, and the calculated vibrational frequencies and intensities for $XeOF_4$ (Table S2); calculated vibrational frequencies, Raman and infrared intensities and assignments for $(\mu\text{-}FOsO_3F_2)_2OsO_3F^-$ (Table S3); natural bond orbital (NBO) charges, valencies, and bond orders for $(\mu\text{-}FOsO_3F_2)_2OsO_3F^-$ (Table S4); experimental and calculated frequencies, intensities and assignments for *cis*-OsO_2F_4 (Table S5); factor-group analysis for $(OsO_3F_2)_2\cdot 2XeOF_4$ (Table S6); calculated geometrical parameters for $(\mu\text{-}FOsO_3F_2)_2OsO_3F^-$ (Table S7); calculated gas-phase geometry for $(OsO_3F_2)_2\cdot 2XeOF_4$ (C_1, SVWN/SDDall) (Figure S2); natural bond orbital (NBO) charges, valencies, and bond orders for $(OsO_3F_2)_2$ and $(OsO_3F_2)_2\cdot 2XeOF_4$ (Table S8); complete references 40 and 43; and a X-ray crystallographic file in CIF format for the structure determination of $(OsO_3F_2)_2\cdot 2XeOF_4$. This material is available free of charge via the Internet at http://pubs.acs.org.

IC900242M

(42) Ehlers, A. W.; Bohme, M.; Dapprich, S.; Gobbi, A.; Hollwarth, A.; Jonas, V.; Kohler, K. F.; Stegmann, R.; Veldkamp, A.; Frenking, G. *Chem. Phys. Lett.* **1993**, *208*, 111–114.
(43) Frisch, M. J. et al. *Gaussian 98*, Revision A.11; Gaussian, Inc.: Pittsburgh, PA, 2003.
(44) *GaussView*, release 3.0; Gaussian Inc.: Pittsburgh, PA, 2003.